AIAA JOURNAL
Vol. 47, No. 1, January 2009

Bluff Body Noise Control Using Perforated Fairings

K. Boorsma* and X. Zhang†
University of Southampton,
Southampton, England S017 1BJ, United Kingdom
N. Molin‡
Airbus, 31060 Toulouse, France
and
L. C. Chow§
Airbus, Filton, Bristol, England BS99 7AR, United Kingdom

DOI: 10.2514/1.32766

Landing gears of commercial aircraft make an important contribution to total aircraft noise in the approach configuration. Using fairings to shield components from high-speed impingement reduces noise. Furthermore, perforating these fairings has been confirmed by flight tests to enable a further reduction. A fundamental study has been performed to investigate and optimize the benefits of bleeding air through the fairing by application of perforations. Experiments have been performed with a simplified fairing–strut combination to clarify the influence of perforations on flow behavior and acoustics. The fairing self-noise is reduced significantly by breakdown of the vortex shedding process, resulting in a reduction of the associated broadband noise level. A redistribution of the velocities is achieved depending on the applied porosity. However, increasing the porosity can result in adverse noise effects due to the bled mass flow washing the strut. Self-noise of the perforations manifests itself at higher frequencies, although scaling of this phenomenon with orifice diameter opens up the possibility to shift it above the upper limit of the audible range.

Nomenclature

D_f	=	shell (outer) diameter, mm
D_s	=	strut diameter, mm
d_{or}	=	orifice diameter, mm
f	=	frequency, Hz
L	=	shell length, mm
p_{or}	=	pitch between orifices (distance between the orifice centerpoints), mm
p_{ref}	=	reference pressure, Pa
$p'(t)$	=	instantaneous sound pressure, Pa
Re	=	Reynolds number
r_{edge}	=	orifice edge radius, m
Str	=	Strouhal number
t_f	=	shell thickness, mm
$\mathbf{u}$	=	velocity vector, m/s
σ	=	open area ratio (ratio of open area over total surface area), %
φ	=	angle from shell leading edge, deg

Subscript

∞	=	freestream conditions

Presented as Paper 3462 at the 13th AIAA/CEAS Aeroacoustics Conference, Rome, Italy, 21–23 May 2007; received 13 June 2007; accepted for publication 8 September 2008.

*Ph.D. Student, School of Engineering Sciences; koenboorsma@yahoo.com.
†Professor, School of Engineering Sciences; xzhang1@soton.ac.uk. Associate Fellow AIAA.
‡Engineer, 316 Route de Bayonne, Post Office Box M0112/4.
§Engineer, Building 09B.

I. Introduction

A STEADY increase in flights and airports has initiated research into aviation noise for commercial aircraft. A more stringent legislation and increased environmental awareness on this subject has led to an extra push. Research started with tackling the most dominant component, engine noise. As a result, engine noise has been reduced dramatically over the past decades, thereby increasing the relative importance of airframe noise for noise certification and environmental considerations.

Landing gear noise can be the dominant component of airframe noise, especially for larger aircraft [1]. However, often none of the various airframe noise sources (flaps, slats, and landing gears) are dominant [2]. In this case total airframe noise can only be reduced significantly if all components are reduced by a similar amount, which makes reduction of landing gear noise essential. Purely designed to perform their main function, landing gears feature an extremely aerodynamically unfriendly shape. The interaction of airflow with protrusions and cavities gives rise to complex unsteady flow phenomena, constituting a potent sound generating mechanism.

Shielding landing gear components with fairings and thereby preventing this interaction has been considered before [1,3]. High-speed flow deflection onto other components and fairing self-noise are disadvantages of this measure. Bleeding air through the fairing results in a redistribution of the airflow. Flight tests using perforated fairings have been conducted before and demonstrated a noise decrease [4,5]. The aim of the present research is to investigate and optimize the noise reduction potential by perforating these fairings.

Previous fluid dynamics research on perforated surfaces focuses on flat plates spanning an entire cross section, originating from the field of hydraulics [6,7]. Empirical formulas have been developed to determine the relationship between perforation characteristics and the pressure drop over the plate. Turbulence characteristics downstream of differently perforated plates have been investigated [8,9] by means of hot wire measurements.

More relevant is the case of perforated or porous plates with finite dimensions, that is, allowing air to pass sideways of the plate. Castro [10] researched a number of perforated plates of finite width spanning the tunnel height in the Reynolds number range between 2.5×10^4 and 9.0×10^4 (based on plate width). Hot wire

measurements in the wake of the plates indicate that above a porosity of 20%, the periodic vortex shedding associated with the plate disappears.

Aeroacoustic research on perforated surfaces mainly concentrates on surface impedance variation [11] and the application of perforated sheets in acoustic liners. The effect of bleeding air through a fairing on aeroacoustic performance of a bluff body is a relatively new topic. The complex shape of the perforations and landing gear fairings make it difficult to perform detailed experimental and computational investigation of acoustics and flow behavior. Therefore experiments are conducted employing a simplified fairing–strut combination.

II. Experimental Setup and Models

A. Test Models

The subject of investigation is a thin walled half-cylindrical shell shielding a cylinder. Because a cylindrical strut does not exhibit small-scale details and irregularities characteristic for landing gear geometry, an acoustic test employing an H beam instead of a cylinder is also performed. A representation of these shapes is shown in Fig. 1.

A number of easily exchangeable shells with different perforations, summarized in Fig. 2, are used to shroud the struts. All perforations are in a hexagonal pattern, which yields a constant pitch between neighboring orifices and a 60 deg angle between lines connecting the orifice centerpoints. The hexagonal pattern has the straight line of holes aligned in the polar direction. The open area ratio (σ) can be defined as the ratio of open surface over total surface measured along the curved contour. For a hexagonal pattern this can be defined as

$$\sigma = \frac{1}{6}\sqrt{3}\pi\left(\frac{d_{\mathrm{or}}}{p_{\mathrm{or}}}\right)^2 \tag{1}$$

where d_{or} is the diameter and p_{or} is the pitch between orifices. The perf42 shell features solid margins to its sides and the perforations do not cover the entire shell. The holes of this shell have been rounded off on the side facing the flow, giving them an approximate edge radius of 0.2 mm.

To determine the influence of perforation location, the perforated shells were partly covered with tape. The tape is attached uniformly in the spanwise direction and symmetrically in the polar direction with respect to the shell leading edge. The angle φ denotes the part of the shell which has perforations exposed to the flow, where φ is defined in Fig. 1a. In the current convention, $\varphi = \pm 30$ deg means that $180 - (2 \times 30) = 120$ deg of the shell is covered with tape while on the remaining area, the perforations are open to the flow. The open area always includes the stagnation point. Hence 0 deg is a fully taped model and ± 90 deg denotes full exposure of the perforations.

B. Test Setup

1. Aerodynamic Measurements

Particle image velocimetry (PIV) and hot wire anemometry measurements were performed in the University of Southampton 3×2 ft^2 wind tunnel. This 12.8-m-long open circuit tunnel exhibits a rectangular (2.5 m long, 0.9 m wide, and 0.6 m high) test section. The model was mounted above a ground plate to span the tunnel vertically and obtain a nominally two-dimensional flow. A coordinate system can be defined originating at the strut center, at a

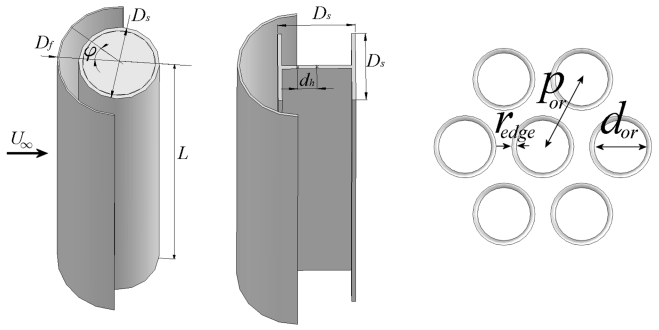

Dimensions		
Shell (outer) diameter	D_f	152 mm
Strut diameter	D_s	100 mm
Shell length	L	514 mm
Cylinder center to shell center	–	0 mm
H-beam center to shell center	d_h	25 mm
Polar angle from shell leading edge	φ	
Orifice diameter	d_{or}	
Orifice pitch	p_{or}	
Orifice edge radius	r_{edge}	

a) Shrouded cylinder **b) Shrouded H-beam** **c) Perforation arrangement** **d) Specification of dimensions**

Fig. 1 Illustration of basic model and dimensions.

Shell	σ (%)	d_{or} (mm)	p_{or} (mm)	Location of perforations (φ)
solid	0	-	-	-
perf33	33	3	5	$\pm 90°$
perf42	42	3.2	4.7	$\pm 45°$
perf55	55	7	9	$\pm 90°$

a) View of different fairings **b) Specification of different fairings**

Fig. 2 Summary of different fairing configurations.

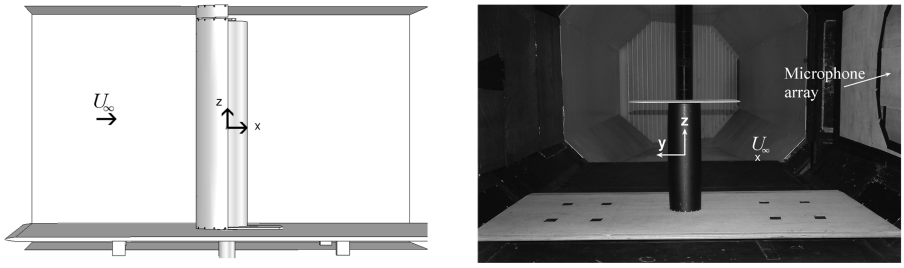

a) Side view of test arrangement in 3′×2′ tunnel b) Front view of test arrangement in 7′×5′ tunnel

Fig. 3 Test setup in wind tunnels.

a) Model suspension and location b) Placement of the microphone arc

Fig. 4 Test setup in the anechoic chamber.

spanwise location halfway across the model. The x, y, and z axes are in the streamwise, transverse, and spanwise directions, respectively. A schematic is shown in Fig. 3a. The flow speed is regulated by a manual operated frequency controller that varies the speed of a fan at the downstream end of the diffuser. This fan speed is set to give a constant pressure difference over the contraction. Flow speed is measured with a pitot–static tube, located upstream at $(x/D_f, y/D_f, z/D_f) = (-6.56, 1.41, 0.89)$. The two tubes are connected to a Furness Controls FC012 digital micromanometer with a range of 2000 Pa. The output of the micromanometer is read by a data acquisition computer after converting the signal using an analog-to-digital converter. By inputting tunnel temperature and pressure, the pressure difference from the micromanometer is converted to velocity using Labview based software.

The high blockage of the tunnel by the model (17%) would barely satisfy requirements to be able to correct for blockage in the case of cylinder flow [12]. The same holds for the necessary aspect ratio to obtain a nominally two-dimensional flow [13]. However, practical considerations limit the parameters to these values and the current investigation will only compare the different configurations of the present experiment. Freestream turbulence levels are approximately 0.2% over the velocity range up to the maximum flow speed of $U_\infty = 30$ m/s [14,15].

2. *Acoustic Measurements*

Measurements with on-surface microphones (flush mounted with the model surface) and a microphone array were performed in the University of Southampton 7×5 ft^2 wind tunnel. Additional acoustic measurements with microphones positioned out of the flow were performed in the anechoic chamber.

7×5 ft^2 *Wind Tunnel:* The closed circuit 7×5 ft^2 wind tunnel at the University of Southampton features a 2.1 m wide, 1.7 m high octagonal cross section. The model was suspended vertically on a ground plate, using a square 500 mm end plate on the model top end as shown in Fig. 3b. Consequently the blockage is approximately 15% of the value in the 3×2 ft^2 tunnel based on the frontal area.

Tunnel speed is measured by a pitot–static tube, located upstream at $(x/D_f, y/D_f, z/D_f) = (-9.70, 6.56, 4.79)$. The dynamic pressure is measured by a Setra model 239 pressure transducer with a range of 1.25×10^3 Pa. Freestream turbulence levels are approximately 0.2% over the velocity range up to the maximum flow speed of $U_\infty = 40$ m/s [16].

Anechoic Chamber: Acoustic measurements with microphones placed out of the flow are performed in the $9.15 \times 9.15 \times 7.32$ m^3 anechoic chamber at the Institute of Sound and Vibration Research [17]. The airstream is provided by a nozzle connected to a compressed air tank through piping as discussed by Chong et al. [18]. The nozzle has a contraction ratio of 10:1 and a rectangular exit of 500 mm high and 350 mm wide. The model was suspended horizontally in front of the nozzle exit as depicted in Fig. 4. Similar to the wind tunnels, a coordinate system can be defined originating in the model center as shown in Fig. 4a. The nozzle exit is located in the yz plane at $x/D_f = -1.67$, while the nozzle center in the yz plane coincides with the model center at $y/D_f = 0$ and $z/D_f = 0$. As shown in the figure, endplates were constructed flush with the sides of the nozzle to prevent the jet from spreading in a spanwise direction and enforce nominally two-dimensional flow behavior. The

endplates were cut to nozzle height and extended 850 mm in the streamwise direction amounting to a total size of $3.28D_f \times 5.58D_f$.

Maximum achievable freestream velocity at the nozzle exit is $U_\infty = 45$ m/s, but because there is a limit to the compressed air, this velocity can be maintained only for a short period of time (less than 30 s). Freestream velocity is measured by a pitot–static tube located at the nozzle exit, at a location of $(x/D_f, y/D_f, z/D_f) = (-1.67, -1.21, -0.36)$. The dynamic pressure is measured by a Comark C9551 pressure meter with a range of 14,000 Pa.

III. Experimental Apparatus

A. Oil Flow Visualization

A mixture of titanium dioxide, paraffin, and oleic acid was applied to the surfaces of the shell and strut in the 7×5 ft tunnel. The oil is transported along surface streak lines leaving an image of the time-averaged flowfield after it has dried up. Flow direction and separation are typical phenomena observed with this technique [19]. However, near to separation lines the oil may pile up to form a steep ramp affecting separation position [20]. The streak line pattern at separation lines depends on the initial condition due to the building up of the oil. In practice this means the pattern is dependent on how much oil was applied. Usually the built up oil leaves a line upstream of the actual separation line. The flow pattern was photographed using a standard digital camera, with the model still present in the tunnel as removing it would disturb the flow pattern.

B. Particle Image Velocimetry

PIV was used to obtain information about the velocity field in an xy plane at the model center. Measurements were performed using a Dantec FlowMap system. A 120 mJ Nd:YAG dual-cavity laser was fixed on a table to the side of the 3×2 ft tunnel, shining through a perspex side window and illuminating a streamwise plane (xy plane) halfway across the model. A water-based seed generator was used to seed the flow, producing a particle size varying between 1 and 5 μm. An 80C60 HiSense charge-coupled device (CCD) camera (1280×1024 pixel resolution) was mounted on slides above the tunnel enabling a streamwise traverse. The camera looked through a 200-mm-wide glass ceiling plate perpendicular to the laser sheet. Using a 24 mm lens, the image size of the planes was around 260×210 mm in the transverse and normal directions, respectively. This necessitated three traverse positions of the camera to visualize $x/D_f \epsilon [-1.04, 2.15]$ with an overlap of 15%. Five hundred image pairs were recorded per configuration. The time between recordings was kept constant at 0.5 s. The time between each pulse varied with flow speed on the order of 50 μs.

The images were postprocessed using FlowManager software [21] provided by Dantec Dynamics. An adaptive correlation was performed with two refinement steps, starting with 128×128 and ending with 32×32 pixel interrogation area size. Vertical and horizontal overlap of the two images in each pair is set to 75%. Erroneous vectors were removed using a range and peak validation. The mean velocity field is obtained by averaging the 500 instantaneous vector maps.

The accuracy of the instantaneous velocity fields can be estimated by assuming an accuracy in the correlation of 0.1 pixel displacement [22]. This corresponds to a maximum error in the velocity of 0.40 m/s. Using error analysis for multisample experiments as described by Moffat [23], the uncertainty in a time-averaged vector is 0.02 m/s.

C. Hot Wire Anemometry

The hot wire probe had a single 2.5-μm platinum-plated tungsten wire. The wire is suspended to a traverse post in the 3×2 ft tunnel, which had the form of a 25-mm-diam metal bar aligned in the z direction. The traverse moves through a slotted gap in the ceiling, sealed airtight by a rubber strip. The probe was connected to a constant-temperature anemometer bridge circuit, manufactured by the University of Newcastle [14]. The output from the bridge was connected to an analog-to-digital converter connected to a data acquisition computer. Labview based data acquisition software is used to document and control the hot wire measurements. To convert the voltage signal to velocity, a calibration was performed in an empty test section against the pitot tube. The hot wire was aligned parallel to the z direction. Therefore it reacted to the velocity components in the x and y directions.

The power spectral density (PSD) of the velocity signal is calculated to investigate unsteady flow features. The hot wire data are sampled at a rate of $f = 20,000$ Hz, taking 50 blocks of $n = 16,384$ samples each, which gives a frequency resolution of 1.22 Hz. The frequencies in the PSD plots are made dimensionless using

$$Str_{D_f} = \frac{fD_f}{U_\infty} \tag{2}$$

The uncertainty of the hot wire measurements depends on a number of factors. The error estimation by Moffat [23] distinguishes fixed and variable sources, depending on whether the error it introduces is steady or changes during the time of one complete experiment. Employing this method, the fixed error consists of the accuracy of the calibration against the pitot–static tube and including the accuracy of the pitot tube itself this adds up to 0.20 m/s. Variable errors are estimated by comparing the mean values of the 50 acquired blocks. The average standard deviation at $U_\infty = 20$ m/s equals 0.35 m/s, indicating an uncertainty of 0.05 m/s for the 50 samples. Adding these values by calculating the root sum square [23] yields a total uncertainty in the velocity measurements of 0.21 m/s at $U_\infty = 20$ m/s. This value is valid outside the wake and shear layer. However, if the wire is traversed into reversed flow (wake) areas, the velocity magnitude of the measurements is not reflected accurately. A qualitative comparison of the velocity spectra is regarded as more suitable. The frequency resolution of 1.22 Hz is a measure for the accuracy of frequencies of the velocity spectra.

D. Microphones

Two different sets of microphones were used in the 7×5 ft wind tunnel and the anechoic chamber. For the wind-tunnel test, microphones with a diameter of 6 mm were flush mounted with the strut surface at various positions. The microphones used are Panasonic Omnidirectional Back Electret Condenser Cartridges, series WM-61A, with a frequency response of 20 Hz–20 kHz. The signals of the electret microphones were sent through preamplifiers built in-house.

For the anechoic chamber tests, Behringer ECM8000 omnidirectional electret microphones were used. They exhibit a response range of 15 Hz–20 kHz and are powered by two 8-Channel DIGIMAX FS preamplifiers, manufactured by PreSonus. The microphones are suspended on a steel frame arc approximately 2 m from the model as depicted in Fig. 4b. The position of the microphones is summarized in Fig. 5a. The angle, defined with respect to the model center in the xy plane, amounts to 90 deg right above the model and increases from the upstream to the downstream quadrant.

For both sets of microphones analog-to-digital conversion was performed using a National Instruments' PXI-4472 24 bit data acquisition card, controlled by a PC using LabView software. A calibration factor was calculated using the recorded signal of a B&K pistonphone (type 4230) to convert the raw data to narrowband spectra with a reference pressure $p_{\text{ref}} = 2 \times 10^{-5}$ Pa. The microphone data of the anechoic chamber experiment were averaged over the microphones (after correcting for the varying distance between model and microphones) to obtain one spectrum for each configuration. The data were sampled at a frequency of $f =$ 48 kHz and a block size of $n = 16384$, averaged over 60 blocks.

The accuracy of the microphone measurements consists of many parts and is hard to estimate. However, microphone levels are predominantly compared between different configurations, thus the fixed error is unimportant. The variable error is estimated by comparing the values of the 60 acquired blocks and adds up to 0.5 dB for both sets of microphones, roughly constant for each frequency band.

Mic number	Angle in xz-centerplane (°)	Distance from model center (mm)
1	56	1800
2	67	1730
3	83	1820
4	101	1830
5	110	1980
6	120	2050
7	130	2170
8	139	2200
9	150	2300
10	156	2340
11	166	2420

a) Position of far-field microphones

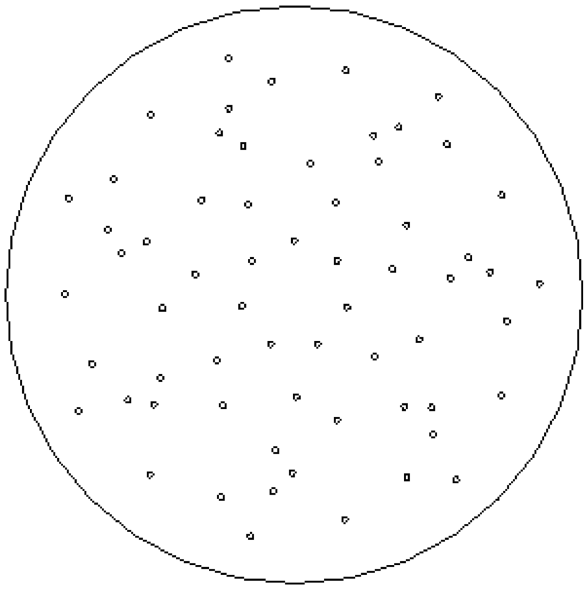

b) Spiral of phased microphone array

Fig. 5 Positioning of microphones.

E. Phased Microphone Array

The phased array consisted of 56 microphones, which were arranged in a spiral as shown in Fig. 5b and mounted flush with the surface on a wooden board with a diameter of 700 mm. The array was mounted flush with the starboard side wall of the 7×5 ft wind tunnel, as partly visible on the right-hand side of Fig. 3b. Because the microphones were placed flush with the tunnel wall, a porous Kevlar® cloth is fixed on the surface of the array board to reduce microphone distortion due to tunnel wall boundary layer noise.

Microphones, data acquisition, and microphone calibration were the same as for the on-surface microphone measurements. However, sampling frequency is set to $f = 48$ kHz, block size to $n = 4096$, and the data were averaged over 100 blocks. The beam-forming code for the present experiments was written by Fenech and Takeda [24] and is based on conventional frequency-domain beam forming [25]. One-third octave band averaged beam-forming plots were calculated for comparison between configurations; however, the finite aperture of the array prevented sufficient resolution for localization below 2 kHz. The absolute level of the contour plots is not physical; however, the difference in level between plots for the same frequency can be interpreted. The scan plane was an xz plane at $y = 0$, which corresponds to the model symmetry plane. For a more quantitative comparison between configurations, the levels of the beam-forming plots were integrated between $x/D_f = \pm 1.0$ and $z/D_f = \pm 1.7$ to give one-third octave band averaged spectra.

The fixed error of the beam-forming plots and their integrated levels is not relevant because they are only used for a comparison between configurations. A rough estimate for the variable error is obtained from a comparison between two runs with identical configurations. This yields a maximum uncertainty of 1.5 dB for the beam-forming plots and 0.45 dB for the integrated levels.

IV. Results and Discussion

A. Reynolds Number

The topology of two-dimensional bluff bodies is often compared to cylinder flow for which flow regimes are well documented [26]. The wind tunnels used in this investigation limit the freestream velocity range between $U_\infty = 20$ m/s and $U_\infty = 40$ m/s, resulting in Reynolds numbers based on shell diameter D_f between $Re_{D_f} \epsilon [2 \times 10^5, 4 \times 10^5]$. The in-flight Reynolds number will be approximately twice this value and hence in the supercritical regime. The proximity of Re_{D_f} to the critical Reynolds number for cylinder flow necessitates application of roughness strips on the solid shell to ensure turbulent separation. However, oil flow and hot wire measurements for a variety of roughness strips (down to grit 60 positioned at $\varphi = \pm 45$ deg) indicate no change in the separation point and shedding behavior for the solid shell. The shell trailing edge at $\varphi = \pm 90$ deg and the presence of the strut fix the shell separation point to approximately $\varphi = \pm 85$ deg for both the solid and perf42 (± 45 deg) configuration. Figure 6 illustrates the separation point location, although separation patterns are different for the two shells.

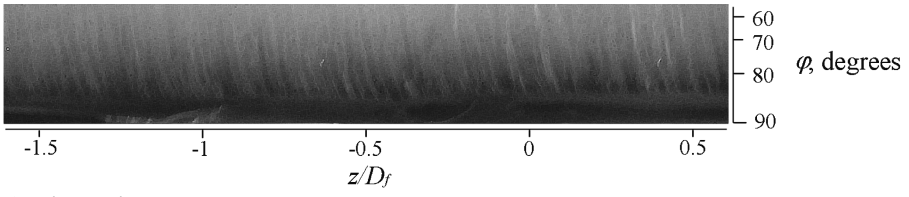

a) solid + cylinder

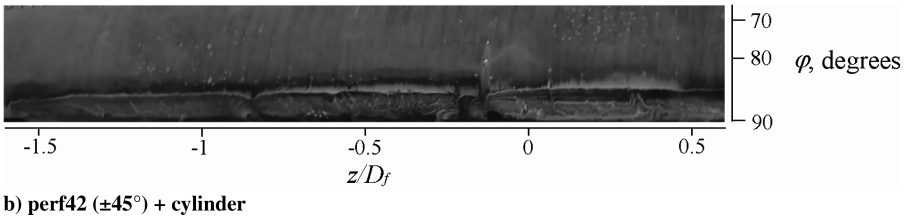

b) perf42 (±45°) + cylinder

Fig. 6 Oil flow visualization at the shell trailing edge ($U_\infty = 40$ m/s), flow from top to bottom.

B. Time-Averaged Flow Features

Oil flow surface visualization in Fig. 6 confirms broadly two-dimensional flow behavior for the attached flow region on the shells. Time-averaged velocity contours obtained by PIV are shown in Fig. 7. For the solid model, a thin high velocity gradient shear layer is present aft of the shell trailing edge. The shear layer rapidly diffuses aft of the shell, thereby shortening the length of the wake downstream of the model. The time-averaged streamlines suggest that the separated flow structure is related to the diameter of the shell.

The low velocity area in the vicinity of the stagnation point for the solid configuration disappears in Fig. 7b due to the air passing through the perforations. The maximum deflected velocities on the shell sides are 18% lower for the perf42 (± 45 deg) configuration. The flow through perforations can be represented by a number of jets that form independently and then gradually spread and coalesce with neighboring jets [7]. The perforations will deflect the flow toward the longitudinal axis of each orifice, hence toward the projected shell center. The fully mixed jets result in isotropic turbulence [7] impinging on the strut. A rough estimate for the bled mass flux through the perforations can be obtained by integrating the velocity of the jet that results from the acceleration between shell and strut in Fig. 7b. Referenced to the freestream flux based on the frontal area of the perforated part of the shell, approximately 32% is bled through. It is the pressure difference between the upstream and downstream sides of the shell that drives the flow through the perforations. Exposing the perforations on the suction side of the shell ($\varphi > 30$ deg) will therefore be less effective for the purpose of bleeding air than the stagnation area perforations. However, this also depends on the pressure variation on the downstream side of the shell.

The accelerated flow that emerges from between the shell and strut significantly alters the wake structure compared to the solid model. Two different shear layers originating from the strut and the shell, respectively, merge and diffuse more slowly resulting in a downstream extended wake. As a consequence, the high velocity region to the side of the strut extends further downstream as well. The magnitude of the maximum velocity gradient relating to the shear layers is roughly 50% of the solid configuration.

C. Vortex Shedding

Turbulence statistics in the form of standard deviation of velocity in the y direction are shown in Fig. 8. For the solid model, the two shear layers interact and roll up to result in high amplitude transverse velocity fluctuations peaking on the centerline of the wake ($y/D_f = 0$). These statistics suggest the existence of large scale vortex shedding associated with the solid fairing. The air bled through the perforations prevents the communication between both shear layers. It acts as a splitter plate and therefore this shedding does not take place. As a consequence, the transverse velocity fluctuations are of significantly lower amplitude and the maxima occur close to the shear layers instead of the centerline.

To investigate the spectral content of the wake, a hot wire is traversed downstream of both models. Results of the traverse are shown in Fig. 9. The wake area ($y/D_f = 0$) is characterized by a broadband spectrum, dominated by the breakdown of turbulence through the energy cascade. The side area ($y/D_f = 1.7$) is dominated by large scale velocity fluctuations associated with the shedding. Distinct peaks arise for the solid model, $Str_{D_f} = 0.24$ more pronounced laterally, and $Str_{D_f} = 0.48$ more in the wake area. The first number is believed to correspond to the vortices being shed from

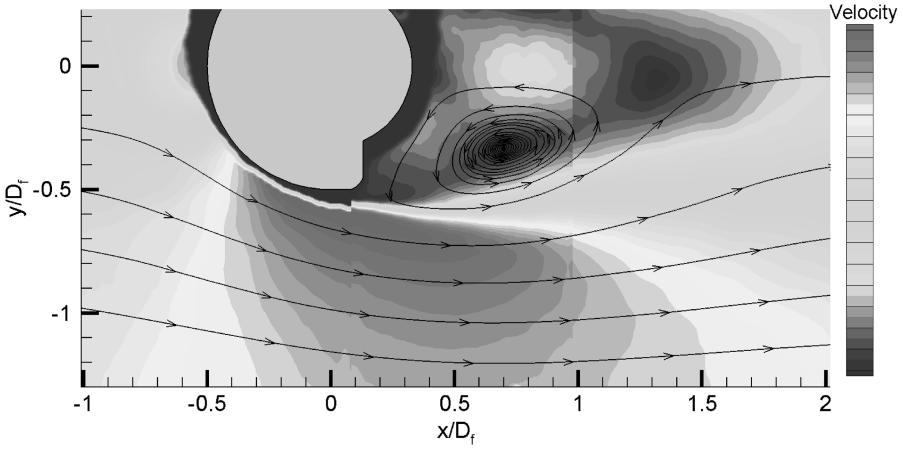

a) solid + cylinder

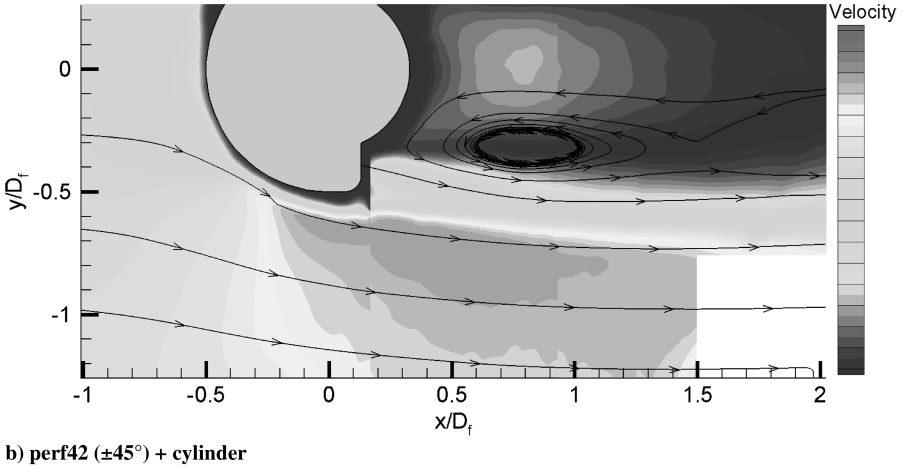

b) perf42 (±45°) + cylinder

Fig. 7 Time-averaged velocity contours and streamlines ($U_\infty = 30$ m/s, $z/D_f = 0$).

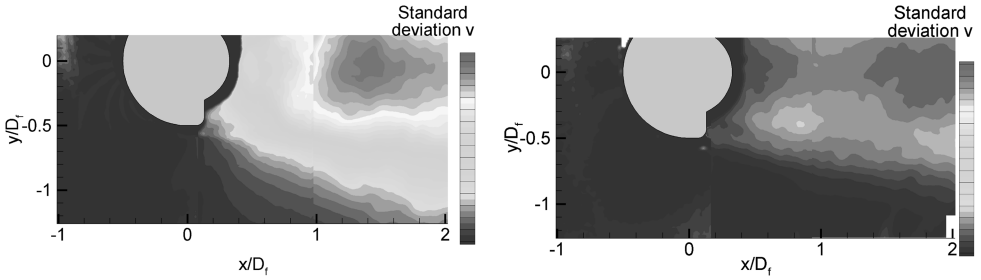

a) solid+cylinder b) perf42 (±45°) + cylinder

Fig. 8 Standard deviation of velocity in the *y* direction ($U_\infty = 30$ m/s, $z/D_f = 0$).

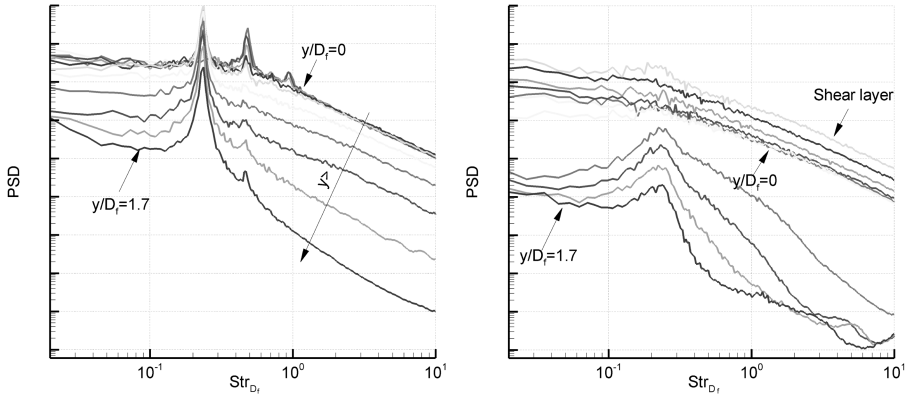

a) solid+cylinder b) perf42 (±45°) + cylinder

Fig. 9 Transverse traverse of PSD of velocity ($U_\infty = 20$ m/s, $x/D_f = 1.44$, and $z/D_f = 0$).

the side of the shell. Because the shedding alternates between each side, double the frequency is more pronounced behind the strut. The dominant frequencies scale linearly with freestream velocity, which conforms with the hypothesized nature of the fluctuations. Although turbulent separation is ensured using roughness strips, it is expected that similar to the supercritical cylinder flow this phenomenon will become less distinct for high Reynolds number flow ($Re_{D_f} > 10^6$) [26]. The same traverse for the perf42 model yields a different graph. To the side a hump instead of a peak is present, indicating less distinct periodicity for this configuration. The fact that the dominant frequency is similar to the solid model indicates that this phenomenon is related to the shell instead of the strut. The level of the PSD is several magnitudes lower for the perforated shell. The largest values of the PSD are concentrated in the merged shear layers, agreeing with the PIV turbulence statistics.

Instantaneous plots of the vorticity field in Fig. 10 agree with the previous observations. The velocity vectors illustrate the existence of large scale vortex shedding for the solid model compared to a small vortex exhibiting approximately half the instantaneous vorticity value for the perf42 (± 45 deg) model.

The quantification of vortex shedding noise in the wind tunnel is hampered by the high background noise levels and the impossibility to suspend the microphones out of the flow. Results from the anechoic chamber experiment are shown in Fig. 11 for both the cylinder and the H beam as shielded objects. The distinct vortex shedding peaks for the solid and isolated cylinder configurations are consistent with the wind-tunnel measurements. Because the cylinder itself is not a noisy object, the level of the solid configuration exceeds the cylinder noise. As confirmed by wind-tunnel measurements, the perforated fairing removes the spectral peak associated with the shedding. Additionally, the broadband noise level is reduced to below the cylinder noise.

Shielding the H beam yields a different image, because this object features many sharp edges and a highly unaerodynamic shape. Therefore the isolated H-beam configuration is far noisier than shielding the beam with the solid fairing. The spectrum exhibits two

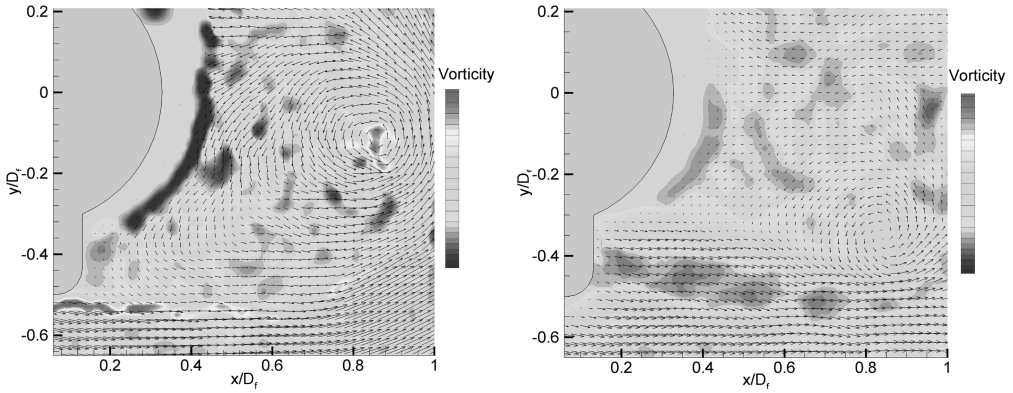

a) solid + cylinder b) perf42 (±45°) + cylinder

Fig. 10 Snapshots of vorticity combined with velocity vectors in the downstream region ($U_\infty = 30$ m/s, $z/D_f = 0$).

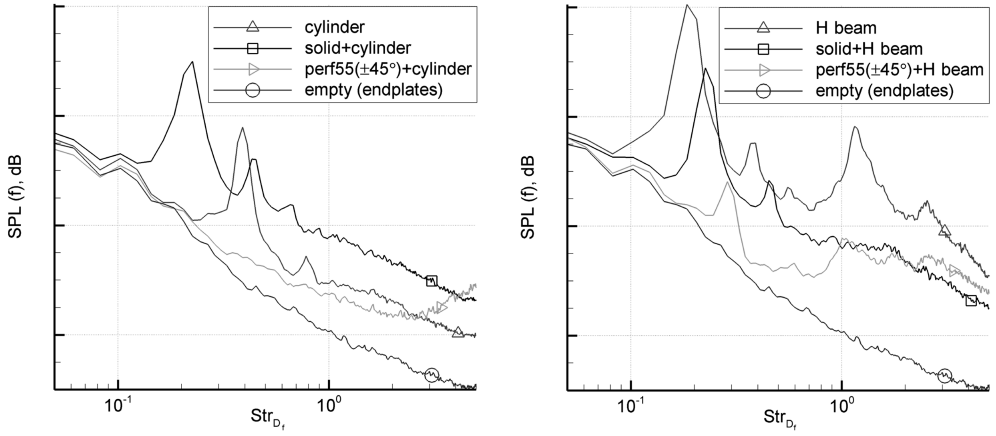

a) Shielded cylinder **b) Shielded H beam**

Fig. 11 Measured acoustic at low frequencies in anechoic chamber ($U_\infty = 40$ m/s).

dominant spectral peaks at $Str_{D_f} = 0.18$ and $Str_{D_f} = 1.20$ that scale with velocity. A comparison of Figs. 11a and 11b indicate that the noise signatures for the solid fairing shielding the cylinder or the H beam are identical. Hence the noise in these cases is dominated by the large scale vortex shedding from the shell, independent of the shielded object. Application of perforations yields further noise decrease, which is most effective at the lowest frequencies.

1. *Effect of Exposure*

Increasing the exposure of the perforations on the perf33 shell starting from an impermeable configuration yields the trends shown in Fig. 12a. For $\varphi = \pm 10$ deg, the distinct peak persists at a slightly higher frequency (increase from $Str_{D_f} = 0.24$ to $Str_{D_f} = 0.30$). To the side of the model, increasing exposure to $\varphi = \pm 20$ deg yields a hump centered around the same frequency. For increasing exposure this humps starts to become less distinct and centered at slightly lower frequencies. This indicates that the flapping of the wake is less unsteady and positions of the shear layers are more stable, due to an increase in the bled mass flux. However, the magnitude of the velocity fluctuations reduces with increasing exposure only up to $\varphi = 60$ deg. It is likely that the pressure difference over the shell between $\varphi = 60$ deg and 90 deg is too small to bleed extra air and reduce unsteadiness.

Figure 13a shows that the results from the anechoic chamber experiment agree with the aerodynamic measurements in the fact that exposing the perforations between $\varphi = 45$ deg and $\varphi = 90$ deg has little effect. However the shielded H beam shows a different trend for increasing exposure. The peak associated with the shedding is not fully broken down for the perf33 (± 45 deg) configuration. It is hypothesized that the difference in cross-sectional geometry is responsible for the discrepancy between the cylinder and the H beam. For the cylinder configuration, the bled air is able to accelerate past the cylinder and form a jet exhibiting high streamwise velocities preventing the occurrence of large scale vortex shedding. For the H beam, the bled flow impinges on the flat surface of the beam, not allowing it to accelerate and develop in a streamwise direction. It is plausible that the orientation of the flat surface in the y direction pushes air through the perforated shell between $\varphi = 45$ deg and $\varphi = 90$ deg. This "blowing mechanism" could distort the shedding and be an explanation for the difference between the $\varphi = \pm 45$ deg and the $\varphi = \pm 90$ deg cases, because the applied tape would prevent this phenomenon in the $\varphi = \pm 45$ deg configuration. The escape of bled flow through the perforations between $\varphi = 45$ deg and $\varphi = 90$ deg implies that the H beam is washed by less mass flow and could therefore be responsible for the decrease in level for $Str_{D_f} > 1$. The perf55 shell shows a similar trend compared to the perf33 configurations, both for the shielded cylinder as for the H beam.

2. *Effect of Porosity*

A comparison between the different porosity shells in Fig. 12b shows few differences between the magnitude of the velocity fluctuations to the side of the model. This indicates that after a certain amount of air is bled through, bleeding more air through the shell becomes less effective for reducing large scale velocity fluctuations. After enough air is bled to break down the vortex shedding, the unsteady flowfield consists of the flapping of the wake in a lateral direction. It appears that this flapping is not significantly altered by increasing the porosity further.

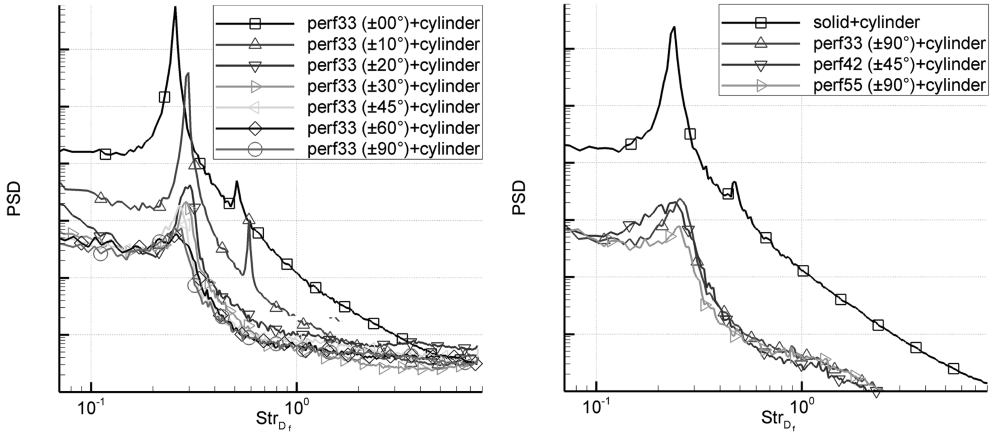

a) Influence of exposure **b) Influence of porosity**

Fig. 12 PSDs of velocity for perf33 + cylinder ($U_\infty = 20$ m/s, $x/D_f = 1.44$, $y/D_f = 1.70$, and $z/D_f = 0$).

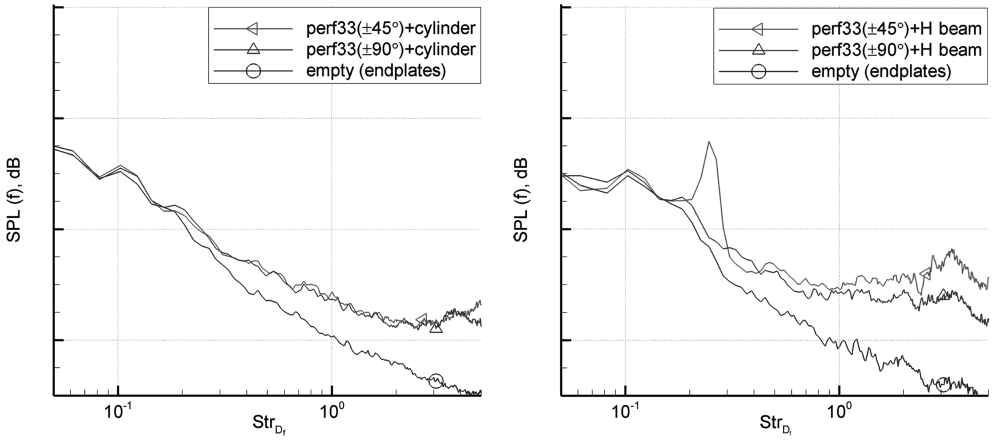

a) Shielded cylinder **b) Shielded H beam**

Fig. 13 Influence of exposure on measured acoustic in anechoic chamber ($U_\infty = 40$ m/s).

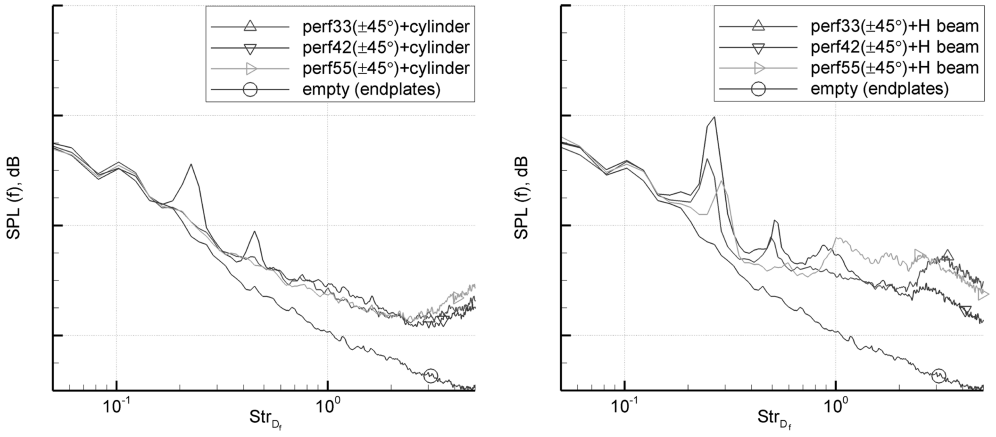

a) Shielded cylinder **b) Shielded H beam**

Fig. 14 Influence of porosity on measured acoustic in anechoic chamber ($U_\infty = 40$ m/s).

Figure 14 shows the effect of varying porosity on the acoustics. The increase in porosity increases the velocity of the bled air past the cylinder. However, the resultant acoustics are not altered by this increase, illustrated by the coincidence of the spectra in Fig. 14a. The cylinder does not exhibit sharp edged or small-scale details that can be responsible for noise creation by high velocity impingement. For the H beam, the increase in bled air does modify the related acoustics. Because the H beam itself is a noisy structure, washing it with higher velocities increases total noise. As soon as the noise source associated with the shedding from the shell is broken down, the H beam becomes the primary noise creation mechanism. This example illustrates the limitations to the perforated fairing concept. The initial purpose of the fairings is to prevent high-speed flow past the landing gear components. Therefore care needs to be taken when applying high porosities to perforated fairings.

D. High-Frequency Noise

Measured noise for several configurations at higher frequencies is displayed in Fig. 15. For both near-field and far-field measurements, a peak occurs in the high-frequency domain at $Str_{D_f} = 35$ for the perf33 model and at $Str_{D_f} = 14$ for the perf55 model. The ratio of these two frequencies is 2.5, which equals the ratio of the orifice diameters of these shells. Comparing the $U_\infty = 40$ m/s data set to the $U_\infty = 20$ m/s and $U_\infty = 30$ m/s data sets also shows scaling with velocity.

Source localization has been performed using the microphone array. Beam-forming plots centered at $Str_{D_f} = 38$ for two different configurations are shown in Fig. 16. The dashed vertical lines represent the strut leading edges, the lower horizontal lines the ground plates, and the upper horizontal lines the endplates. The plots reveal the noise source location at the perforations. A closer look at the differently taped configurations for the perf33 model shows the source moving more downstream from the $\varphi = \pm 30$ deg to the $\varphi = \pm 90$ deg configuration with a corresponding increase of 12 dB. These observations feed the hypothesis that the high-frequency peaks are related to flow resonance ("whistling" or "singing") of the perforations. Grazing flow past sharp edges is known to create an edge-tone–type noise as described by Brown [27,28]. It is most probably this feedback mechanism that is responsible for the perforation noise.

The perf55 model shows a similar behavior at $Str_{D_f} = 15$ with a noise increase of 12 dB between $\varphi = \pm 30$ deg and $\varphi = \pm 90$ deg. The difference between the various taped configurations for the perf55 model becomes clearly visible in Fig. 17a. The level of the maxima as well as the corresponding frequency of the perforation noise shifts with exposure angle φ for each configuration. This illustrates the scaling of the noise with local shearing flow velocity past the perforations. To characterize the frequency content of the noise, the Strouhal numbers based on orifice diameter d_{or} and local velocity can be calculated using

$$Str_{d_{\text{or}}} = \frac{f d_{\text{or}}}{u} \tag{3}$$

The orifice diameter is known and the local velocity can be estimated using PIV. The frequencies are estimated from the maxima of the several configurations in Fig. 17a. This yields a rough estimate of $Str_{d_{\text{or}}} \approx 0.33$ for the frequency content of the perforation noise.

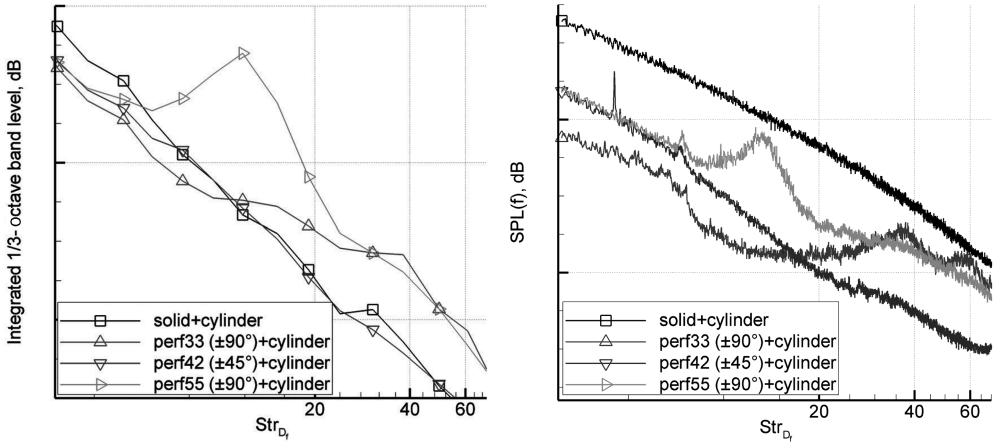

a) Integrated 1/3 octave band averaged beam-forming plots ($x/D_f = \pm 1.0$ and $z/D_f = \pm 1.7$)

b) Narrowband spectra of microphone in the cylinder surface ($\varphi = 160^o$, $z/D_f = -0.14$)

Fig. 15 Measured acoustics at high frequencies in 7 × 5 ft tunnel ($U_\infty = 40$ m/s).

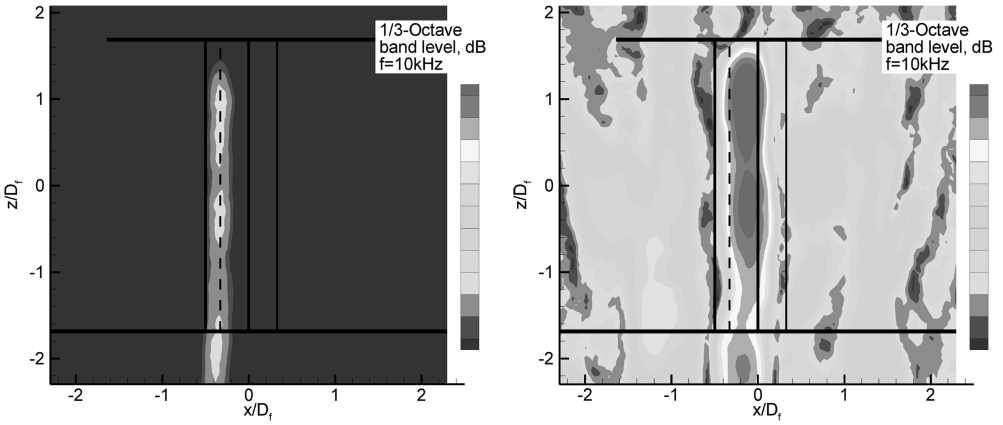

a) perf33 (±30°) + cylinder, $Str_{D_f} = 38$

b) perf33 (±90°) + cylinder, $Str_{D_f} = 38$

Fig. 16 Source location on perforation noise by one-third octave band averaged beam-forming plots ($U_\infty = 40$ m/s).

Although the perforation noise does not emerge for the perf42 (±45 deg) configuration in Fig. 15, the beam-forming plots do reveal the noise in Fig. 17b. However, the level of the noise is 8 dB lower compared to the perf33 (±45 deg) model exhibiting a similar orifice diameter. The hole edge radius of the perf42 shell perforations (versus the sharp hole edge for the perf33 shell perforations) is responsible for the reduced intensity of the noise.

To extrapolate the frequency range to flight conditions, one should take into account size and velocity changes. Typical speed during approach is $U_\infty = 80$ m/s. Assuming the magnitude of the shearing flow component is $1.5U_\infty$ together with an orifice diameter of $d_{or} = 2$ mm results in frequencies close to the upper limit of the audible range ($f \epsilon [20, 20 \times 10^3]$ Hz). This illustrates the possibility for tailoring d_{or} to avoid the high-frequency noise penalty. In

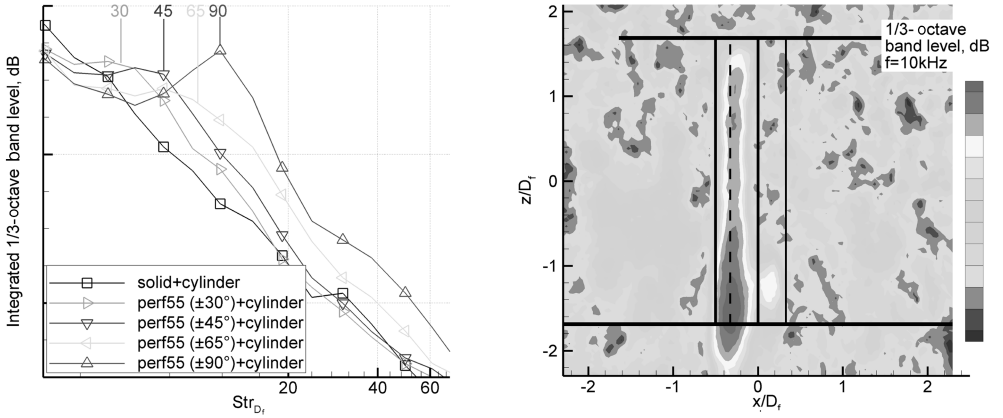

a) Integrated 1/3 octave band averaged beam-forming plots ($x/D_f = \pm 1.0$ and $z/D_f = \pm 1.7$)

b) 1/3 octave band averaged beam-forming plot, perf42(±45°) + cylinder, $Str_{D_f} = 38$

Fig. 17 Characteristics of perforation noise ($U_\infty = 40$ m/s).

addition to that, atmospheric attenuation (along the path between airplane and receiver) will reduce high-frequency noise relative to lower frequencies, because absorption increases considerably with frequency.

V. Conclusions

Experiments with a simplified fairing–cylindrical strut model have been performed to investigate the use of perforated fairings for passive noise control. Both aerodynamics and the related acoustics are studied employing two different wind-tunnel facilities and an anechoic chamber.

Application of perforated fairings shows two shear layers exhibiting roughly half the vorticity of the solid fairing, resulting in weaker vortices of the smaller scale. The distinct spectral peak of velocity fluctuations related to the vortex shedding disappears. However, it is expected that as is the case for supercritical cylinder flow, the periodic shedding of the solid fairing will become less distinct for high Reynolds number flow ($Re_{D_f} > 10^6$). The perforations that are located nearer to the trailing edge of the shell bleed less air and are therefore less effective in reducing the magnitude of the large scale velocity fluctuations. The bleeding of air through the perforations results in a downstream extended wake.

Flow velocities to the side of the shell are reduced because of the bled mass flux through the perforations. Quantitatively, a fairing exhibiting 42% porosity reduces the maximum flow velocity by 18% resulting in a reduction of unwanted high-speed flow deflection by the fairing. A rough estimate of the bled mass flux has been given.

Application of the perforations results in a breakdown of the vortex shedding noise at $Str_{D_f} = 0.2$, illustrated by a vanishing spectral peak in the wind-tunnel measurements. The anechoic chamber test results show that the associated broadband level is reduced as well. Furthermore, a test with a noisy H beam replacing the cylinder indicates that increasing the porosity can result in a noise increase due to the bled mass flow washing the strut.

Finally, the perforations are shown to create noise at higher frequencies centered around $Str_{d_{or}} = 0.33$. The shearing flow past the perforations, tangential to the outer shell surface, is responsible for the high-frequency noise. Both intensity and spectral content are dictated by the local velocity past the perforations and the orifice diameter. This opens up the possibility for tailoring this noise phenomenon above the upper limit of the audible range.

Acknowledgments

Koen Boorsma is supported by a studentship from the School of Engineering Sciences, University of Southampton, United Kingdom. The research is funded by Airbus. Furthermore, the authors would like to thank Benjamin Fenech for his assistance during the acoustic measurements.

References

[1] Dobrzynski, W., and Buchholz, H., "Full-Scale Noise Testing on Airbus Landing Gears in the German Dutch Wind Tunnel," AIAA Paper 97–1597, 1997.

[2] Lopes, L. B., Brentner, K. S., Morris, P., Lilley, G., and Lockard, D., "Complex Landing Gear Noise Prediction Using a Simple Toolkit," AIAA Paper 2005–1202, 2005.

[3] Dobrzynski, W., Chow, L., Guion, P., and Shiells, D., "A European Study on Landing Gear Airframe Noise Sources," AIAA Paper 2000–1971, 2000.

[4] Piet, J.-F., Chow, L., Laporte, F., and Remy, H., "Flight Test Investigation of High-Lift Devices and Landing Gear Modifications to Achieve Airframe Noise Reduction," *Proceedings of the European Congress on Computational Methods in Applied Sciences and Engineering (ECCOMAS 2004)*, 24–28 July 2004.

[5] Piet, J.-F., Davy, R., Elias, G., Siller, H., Chow, L., Seror, C., and Laporte, F., "Flight Test Investigation of Add-On Treatments to Reduce Aircraft Airframe Noise," AIAA Paper 2005–3007, 2005.

[6] Idelchik, I., *Handbook of Hydraulic Resistance*, 2nd, revised, and augmented edition, Hemisphere Publishing Corp., Washington, D.C., 1986, pp. 145–402.

[7] Baines, W., and Peterson, E., "An Investigation of Flow Through Screens," *Journal of Applied Mechanics*, Vol. 73, July 1951, pp. 467–478.

[8] Checkel, M., "Measurements of Turbulence Generated by 60% Solid Perforated Plates," *The Winter Annual Meeting of ASME*, American Society of Mechanical Engineers, Fairfield, NJ, 1985.

[9] Liu, R., Ting, D., and Rankin, G., "On the Generation of Turbulence with a Perforated Plate," *Experimental Thermal and Fluid Science*, Vol. 28, 2004, pp. 307–316. doi:10.1016/S0894-1777(03)00106-7

[10] Castro, I., "Wake Characteristics of Two-Dimensional Perforated Plates Normal to an Air-Stream," *Journal of Fluid Mechanics*, Vol. 46, No. 3, 1971, pp. 599–609. doi:10.1017/S0022112071000727

[11] Akishita, S., and Yahathugoda, I., "Effect of Surface Impedance for Reducing Sound from Circular Cylinder," AIAA Paper 2005–2914, 2005.

[12] West, G., and Apelt, J., "The Effects of Tunnel Blockage and Aspect Ratio on the Mean Flow Past a Circular Cylinder with Reynolds Numbers Between 104 and 105," *Journal of Fluid Mechanics*, Vol. 114, 1982, pp. 361–377. doi:10.1017/S0022112082000202

[13] Zdrakovich, M., *Flow Around Circular Cylinders*, Vol. 2, Applications, Oxford Science Publications, New York, 2003.

[14] Castro, I., *Hot Wire Anemometry with the Newcastle, NSW Bridges*, University of Southampton, School of Engineering Sciences, Aerodynamics and Flight Mechanics Research Group, Nov. 2001.

[15] Webb, S., and Castro, I., "PIV, LDA & HWA Comparative Measurements in Various Turbulent Flows," University of Southampton, School of Engineering Sciences, TR AFM 03/01, 2003.

[16] Davies, P., "The New 7 by 5 1/2 ft. and 15 by 12 ft. Low Speed Wind Tunnel at the University of Southampton," University of Southampton, Department of Aeronautics and Astronautics, TR AASU 202, 1961.

[17] Anon., *An information Booklet About the Test Laboratories (Lab Users Guide)*, ISVR Consulting, University of Southampton.

[18] Chong, T., Joseph, P., and Davies, P., "Design of a Quiet Open Jet Facility for the Measurement of Airfoil Noise," AIAA Paper 2007–3437, 2007.

[19] Smits, A., and Lim, T., *Flow Visualization: Techniques and Examples*, Imperial College Press, London, 2000, pp. 1–24.

[20] Merzkirch, W., *Flow Visualization*, Academic Press Inc. (London) Ltd., London, 2nd ed., 1987.

[21] Dantec Dynamics A/S, Tonsbakken 18, DK-2740 Skovlunde, Denmark, *FlowManager Software and Introduction to PIV Instrumentation*, Sept. 2002, Publication No. 9040U3625.

[22] Raffel, M.,Willert, C., and Kompenhans, J., *Particle Image Velocimetry, A Practical Guide*, Springer–Verlag, Berlin, corrected 3rd printing edition, 2000.

[23] Moffat, R., "Describing the Uncertainties in Experimental Results," *Experimental Thermal and Fluid Science*, Vol. 1, 1988, pp. 3–17. doi:10.1016/0894-1777(88)90043-X

[24] Fenech, B., and Takeda, K., "SotonArray: Southampton University Wind Tunnel Microphone Array System Guide," University of Southampton, School of Engineering Sciences, TR AFM 07/03, 2007.

[25] Humphreys, W., Jr., Brooks, T., Hunter, W., Jr., and Meadows, K., "Design and Use of Microphone Arrays for Aeroacoustic Measurements," AIAA Paper 98–0471, 1998.

[26] Zdrakovich, M., *Flow Around Circular Cylinders*, Vol. 1, Fundamentals, Oxford Science Publications, New York, 1997, pp. 163–203.

[27] Brown, G., "The Vortex Motion Causing Edge Tones," *Proceedings of the Physical Society, London*, Vol. 49, No. 5, 1937, pp. 493–507. doi:10.1088/0959-5309/49/5/306

[28] Brown, G., "The Mechanism of Edge-Tone Production," *Proceedings of the Physical Society, London*, Vol. 49, No. 5, 1937, pp. 508–521. doi:10.1088/0959-5309/49/5/307

C. Bailly
Associate Editor